NANO LETTERS

2009
Vol. 9, No. 5
1909-1915

Mediating Tumor Targeting Efficiency of Nanoparticles Through Design

Steven D. Perrault,[†] Carl Walkey,[†] Travis Jennings,[†] Hans C. Fischer,[‡] and Warren C. W. Chan*[,†,‡]

Institute of Biomaterials and Biomedical Engineering, Terrence Donnelly Centre for Cellular and Biomolecular Research, Materials Science and Engineering, University of Toronto, 160 College Street, Toronto, ON, M5S 3E1, Canada

Received January 5, 2009; Revised Manuscript Received February 18, 2009

ABSTRACT

Here we systematically examined the effect of nanoparticle size (10−100 nm) and surface chemistry (i.e., poly(ethylene glycol)) on passive targeting of tumors in vivo. We found that the physical and chemical properties of the nanoparticles influenced their pharmacokinetic behavior, which ultimately determined their tumor accumulation capacity. Interestingly, the permeation of nanoparticles within the tumor is highly dependent on the overall size of the nanoparticle, where larger nanoparticles appear to stay near the vasculature while smaller nanoparticles rapidly diffuse throughout the tumor matrix. Our results provide design parameters for engineering nanoparticles for optimized tumor targeting of contrast agents and therapeutics.

A central focus in nanomedicine research is the development of sub-100 nm structures as contrast agents, delivery vehicles, or therapeutics for improving the diagnosis and treatment of cancer. Recent studies have successfully demonstrated selective targeting of engineered nanostructures (e.g., quantum dots,[1,2] fullerenes,[3] and gold nanoparticles[4,5]) to tumors. For such nanostructures to advance toward clinical use, there is a need to understand how they interact with the biological systems in question in order to optimize their diagnostic sensitivity, payload, or therapeutic efficiency, respectively. The central premise of targeting nanoparticles to tumors arises from the discovery of their interesting pathology and morphology of tumors. Tumors have immature and porous vasculature, which provides access to circulating particles.[6−8] This finding initiated an interest in developing nanometer-sized vehicles to more efficiently deliver diagnostic and therapeutic agents. Currently, only a handful of therapeutic formulations have been designed to exploit tumor vessel hyperpermeability even after two decades of research.[9,10] The engineering parameters to build efficient delivery vehicles for tumor targeting have not been thoroughly identified since few studies have systematically evaluated the influence of the dimensional, physical, or chemical properties of engineered nanostructures on tumor targeting behavior.

The recent focus of nanotechnology research in cancer biology has begun to provide a fundamental understanding of how nanoparticles interact with biological systems. This fundamental information is necessary to allow for a rational design of nanodelivery systems. Various in vitro studies have demonstrated that nanoparticle size and surface chemistry greatly impact how they interact with plasma proteins,[11] cellular uptake,[12−14] toxicity,[15,16] and molecular response.[17] However, the in vivo environment is far more complex than in vitro model systems, and few studies have investigated the in vivo behavior of engineered nanostructures. Discher et al. examined blood clearance and tumor accumulation of filamentous versus spherical micelles, which were found to influence both the delivery and therapeutic efficiency of the anticancer drug Paclitaxal.[18] Because they did not test a wide array of sizes and aspect ratios, it would be difficult to extrapolate their findings to other nanostructures.

In this study we systematically examine how particle design can be optimized toward efficient tumor targeting. Using an array of particle sizes and surface chemistries, we first test how these parameters impact blood compartment pharmacokinetics (PK). We then measure particle size-dependent tumor accumulation and demonstrate a correlation to blood PK. Finally, the particle size-dependent permeation of the tumor mass is examined, revealing a difference in behavior over the 20−100 nm size range. Through these systematic studies, we demonstrate that particle design has tremendous consequences on tumor targeting behavior, which will allow for an optimized approach to controlling delivery.

Pegylated gold nanoparticles (GNP) are an ideal system to map in vivo behavior of sub-100 nm particles as they are nontoxic,[19] are produced as monodispersed batches, and can

* To whom correspondence should be addressed. E-mail: warren.chan@utoronto.ca.
[†] Institute of Biomaterials and Biomedical Engineering, Terrence Donnelly Centre for Cellular and Biomolecular Research.
[‡] Materials Science and Engineering.

10.1021/nl900031y CCC: $40.75
Published on Web 04/03/2009

Table 1. Nanoparticle Characteristics and in Vivo Behavior

	core diameter (nm) (±SD)	mPEG weight (Da)	hydrodynamic diameter (nm)	blood half-Life (h)	tumor AUC (particle mass (ug)·h/g)	tumor AUC (% ID·h/g)
particle set A	17.72 (1.47)	2000	25.2	4.0		
		5000	34.8	29.7		
		10000	63.5	51.1		
	31.28 (4.83)	2000	42.8	2.4		
		5000	62.6	19.3		
		10000	77.5	22.7		
	45.03 (4.83)	2000	53.8	0.4		
		5000	60.4	14.1		
		10000	83.9	16.1		
	66.54 (5.69)	2000	75.7	1.0		
		5000	85.6	9.2		
		10000	105.8	11.3		
	86.73 (7.74)	5000	105.4	3.3		
		10000	118.9	6.6		
particle set B	16.6 (1.80)	2000	22.4	2.5	0.45	0.3
	22.6 (2.68)	2000	39.6	4.0	18.89	15.8
	32.5 (5.16)	5000	61.3	16.5	39.05	26.5
	43.3 (5.08)	10000	82.6	11.6	39.33	20.4
	83.5 (8.29)	10000	99.4	7.2	170.42	17.9

be easily modified to present different surface chemistries. Steric stabilization of particles with a methoxy-poly(ethylene glycol) (mPEG) surface brush layer is commonly utilized to create long-circulating particles, which reduces the adsorption of reticuloendothelial system (RES) factors in the blood to the particle surface and the rate of clearance of particles by cells of the monophagocytic system (MPS).[20] In the case of gold nanoparticles, thiol-terminated mPEG molecules provide a stable brush layer through co-ordination of the thiol functional group with the gold particle surface.[5]

We synthesized two sets of mPEG-GNP to use throughout this study (see Table 1). The first set, used to map blood PK, is an array of 5 particle sizes and 3 different thiol-terminated mPEG molecular weight brush layers. The largest particle diameter and lowest molecular weight mPEG combination aggregated during pegylation, and therefore only 14 particle designs in total were examined. The results from this first study were used to design a second set of particles, used to test size-dependent tumor accumulation and permeation. This second set of particle designs included 5 combinations of particle diameter and mPEG molecular weight having final hydrodynamic diameters of approximately 20, 40, 60, 80, and 100 nm. All of the synthesized particles were characterized by transmission electron microscopy and dynamic light scattering (see Figures S1 and S2 in Supporting Information). ζ-Potential was measured for all particle designs before and after addition of the mPEG brush layer. Reduction of ζ-potential to near zero was used to verify that the pegylation process was successful.

To allow for a highly sensitive detection of the mPEG-GNP in tissues, we optimized a quantitative sandwich enzyme-linked immunosorbant assay (ELISA) for measuring the concentration of nanoparticles in tissue homogenates. Our assay is highly sensitive, having a lower limit of detection of 0.01% of the injected dose in 5 mg of tissue. It is also highly specific, detecting only pegylated particles and not free mPEG in solution. Desorption of the thiol-mPEG brush layer can occur over time, which would greatly affect particle stability in vivo as well as our ability to detect them via an ELISA.[21] We therefore incubated mPEG-GNP in phosphate buffered saline (PBS) pH 4.0 to pH 9.0 for 48 h, verifying the stability of their mPEG brush layer and the ELISA detection signal for a length of time comparable to our in vivo incubations (see Figure S3a in Supporting Information). We also verified that nonspecific protein adsorption would not interfere with particle detection by comparing detection of particles incubated in 100% fetal bovine serum for 48 h to those incubated in PBS (see Figure S3b in Supporting Information).

The array of 14 particle designs (particle set A, see Table 1) was used to measure how blood half-life changes over a range of particle size and surface mPEG molecular weight. Single bolus injections of the 14 particle designs containing a consistent hydrodynamic surface area (5×10^{15} nm^2) were injected intravenously (IV) into CD1 mice ($n = 4$). We reasoned that interactions between the particles and biological systems (i.e., blood components) would occur at the particle surface, and therefore a constant surface area across particle designs would provide the best basis for comparison. Prior research has shown that clearance by the RES cells in the liver and spleen of rats becomes saturated when more than 10^{15} particles are injected in a single bolus.[21] All the injection doses used here contain at least 1000 times fewer particles and the organ weight of mice is approximately one-tenth that of rats, such that clearance should not be compromised by saturation.

We obtained small volumes of blood at set times postinjection for measurement of particle content. We then calculated PK parameters and mapped each design's blood half-life against the design parameters of core size and mPEG molecular weight (see Figure 1a). Particle half-life in circulation improved with smaller particle diameters and larger mPEG. Half-life was 8 times greater when the same mPEG (10 kDa) was applied to 17 nm particles ($t_{1/2} =$ 51.1 h), compared to 86 nm particles ($t_{1/2} = 6.6$ h). Half-life also increased for each particle size as mPEG molecular weight increased. The 14 times average improvement between particles with mPEG 5 versus 2 kDa was much greater than the 1.5 times improvement between mPEG 10 versus 5 kDa ($p < 0.05$). These effects of size and surface chemistry on PK are similar to what has been reported for

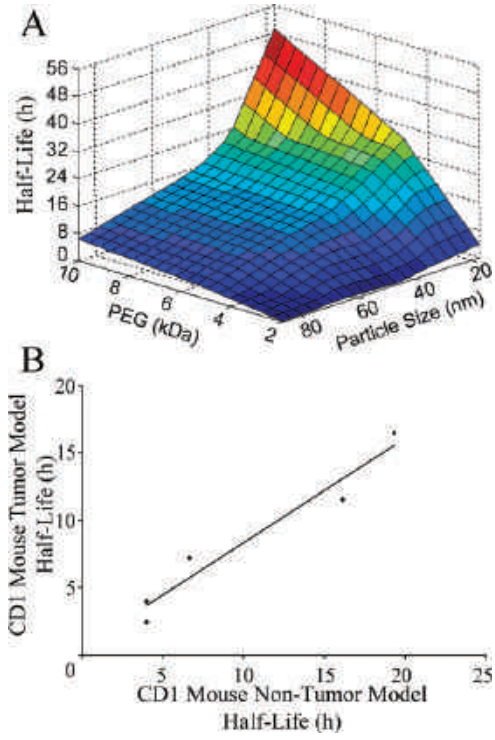

Figure 1. Blood compartment pharmacokinetics and correlation of particle design half-lives across in vivo models. (A) A combination of 5 GNP diameters and 3 mPEG molecular weight brush layers were used to determine blood half-life (hours) as a function of particle size (nm) and mPEG molecular weight (kDa). Half-life generally improved as particle diameter decreased and mPEG molecular weight increased. (B) Blood half-life of the two GNP systems used for PK and biodistribution data were found to correlate ($p < 0.01$).

larger particle systems.[22,23] Fang et al. described PK parameters for a system of particles ranging from 80 to 240 nm, where pegylated 80 nm particles had a similar half-life ($t_{1/2}$ = 11.33 h) to a comparable GNP design tested here ($t_{1/2}$ = 9.24 h). From these results, it follows that the particle size- and surface chemistry-dependent PK trends that previous studies have described for larger particles can be extended to the sub-100 nm region. This also suggests that blood half-life can be maximized by the use of sub-100 nm particles.

Tumor targeting vehicles must be small enough to access the tumor through transvascular pores and fenestrations, making particle diameter central to design. Therefore, we next examined the design-dependent tumor targeting capacity of sub-100 nm particles. Pore cutoff sizes have been measured for a limited number of tumor models with the smallest reported at 100−200 nm.[24,25] On the basis of our results from PK mapping, we designed, synthesized, and characterized a second set of particles having hydrodynamic diameters of approximately 20, 40, 60, 80, and 100 nm (see Table 1 and Figure S2 in Supporting Information). We scaled the ratio of mPEG and particle size, attempting to limit differences in behavior to blood PK and hydrodynamic diameter. Athymic nude CD1 mice bearing 1 cm^3 subcutaneous MDA-MB-435 xenograft tumors were randomly sorted between particle design groups (n = 3) and were then injected IV with a single bolus of mPEG-GNP. At various time points up to 48 h, three animals for each particle design were euthanized, and tissues were collected for analysis.

This second set of mPEG-GNP had half-lives consistent with similar designs used in our PK study ($p < 0.01$, see Figure 1B, and Figure S4 in Supporting Information). The blood half-life of the 60 nm particles was 16.5 h, 6.5 times longer than that of the 20 nm particles, due to its larger mPEG brush layer (5 kDa versus 2 kDa). The 80 nm (11.5 h) and 100 nm (7.2 h) mPEG 10 kDa designs had half-lives of 70% and 44% of the 60 nm, respectively. This has implications for particle design. Half-lives can be improved by larger mPEG molecular weight brush layers, but this also increases hydrodynamic diameter which could impact their ability to extravasate into and permeate through the tumor space. From a design perspective, small hydrodynamic diameter and long half-lives appear to converge when particles below 50 nm are protected with an mPEG layer of moderate molecular weight (MW 5 kDa in our case).

Accumulation of particles and macromolecules in the tumor compartment competes against uptake and clearance by MPS cells. Particle content in the liver (see Figure 2A) and spleen (see Figure 2B) increased over time for all particle sizes. The spleen contained more than liver when normalized per gram of tissue, suggesting a greater filtering efficiency. Because nonspecific uptake of particles can occur in phagocytic cell populations and dense capillary beds present in nontarget organs, we also examined heart and lung tissue. We observed low levels of particle uptake in nontarget organs, but without any consistent trend between particle sizes. The 20 nm particles were cleared rapidly from the blood (see Figure S4 in Supporting Information), yet without a corresponding accumulation in the liver and spleen. They are also unlikely to be cleared via the kidney which has a hydrodynamic diameter cutoff of approximately 6 nm.[26] These particles could have accumulated in peripheral MPS cells, in the lymph following extravasation into nonspecific tissues, or could have been cleared into the intestines via the liver's bile duct. A thorough examination of how particle design impacts nonspecific biodistribution would be important and merits further investigation in follow-up studies.[27]

Particle accumulation in the tumor environment is a critical aspect of vehicle design, as it determines the potential impact of a diagnostic or therapeutic on the tumor mass. Particle accumulation in the tumor was calculated as the area-under-the-curve (AUC), both by the measured % ID/g over time and particle mass/g over time (see Table 1, Figure 2C, and Figure S5 in Supporting Information). The various design sizes showed different degrees of accumulation with the 60 nm particles providing the greatest AUC by % ID at 26.47% ID•h/g, 87.3 times greater than the 0.3% ID•h/g measured for the 20 nm particles. The largest sizes of 80 and 100 nm also had significant accumulation at 20.4 and 17.0% ID•h/g, respectively. Examining accumulation by particle mass, the 100 nm particles achieved the greatest accumulation at 170 ug•h/g. This is 4.3 times greater than that achieved by both the 60 and 80 nm particles, 9 times greater than the 40 nm particles, and 38 times greater than the 20 nm particles. As a measure of potential payload that can be delivered, the

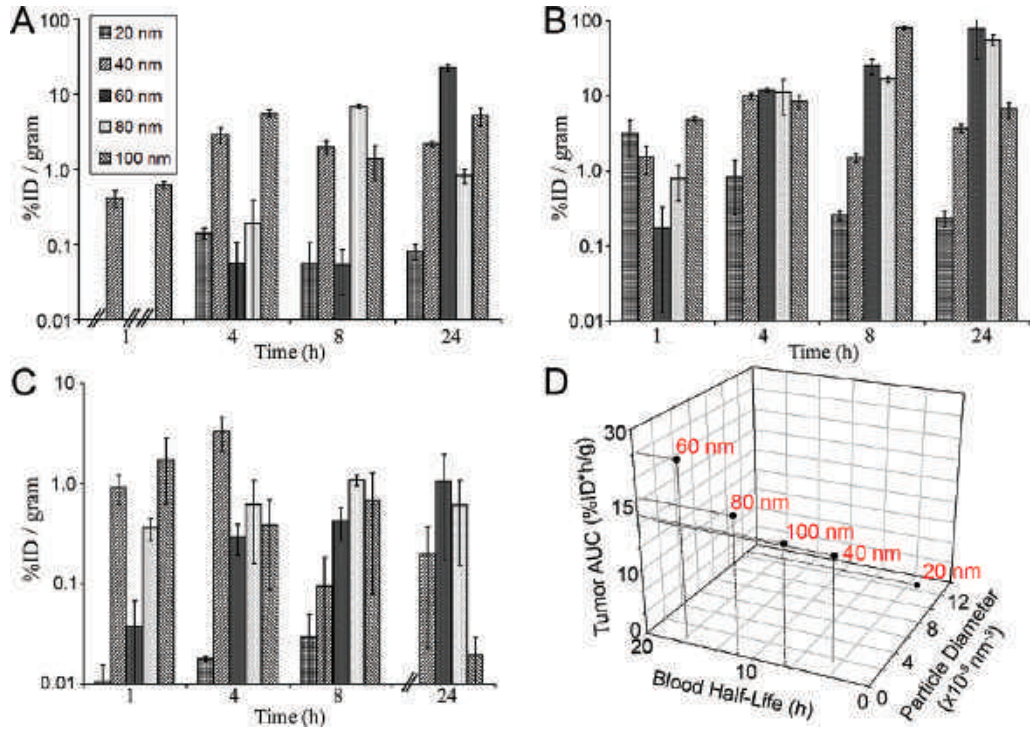

Figure 2. Reticuloendothelial system organ uptake, tumor accumulation, and correlation of particle design to tumor accumulation. (A) Time-dependent liver and (B) spleen accumulation (% ID/g) of the mPEG-GNP designs. A detection signal at or below the negative control, indicating no particle content, is shown with double strikes through the *x*-axis. Uptake of particles was higher in spleen than liver when normalized per gram of tissue. There was a general trend of increasing accumulation in these organs over time. (C) Time-dependent tumor accumulation (% ID/g) of the five mPEG-GNP sizes at 1, 4, 8, and 24 h. Additional time points were measured up to 48 h for treatments with longer half-lives (data not shown). Total tumor accumulation was calculated as area-under-the-curve using a trapezoidal method. (D) Linear regression analysis discovered that total tumor accumulation (% ID•h/g) of the five mPEG-GNP designs is a function of their blood half-life (hours) and of size (nm^{-3}).

100 nm particles would therefore carry the greatest total mass to the tumor owing to their larger volume.

Evidently, all sizes can access the tumor microenvironment in this tumor model. This is expected, given that the pore cutoff size previously reported for other cell lines is between 100 and 200 nm. As well, the MDA-MB-435 human breast cancer cell line used here has been characterized as having very high vascular permeability relative to other breast cancer cell lines, although no pore cutoff size has been described.[28] While there is no clear trend, the difference in accumulation between particle designs (% ID•h/g) is intriguing. Tumor accumulation is a function of both the rate of extravasation from the blood to the tumor space and also the rate of clearance from the tumor. Hobbs et al. showed that the rate of extravasation of bovine serum albumin (BSA) was independent of pore size over a variety of tumor models.[24] This demonstrates that for a 7 nm molecule, which is much smaller than the transvascular pore, extravasation is not dependent on pore size but is instead a diffusive process that will depend on the concentration gradient between blood and tumor. In our model, the absence of size-dependent effects should be reflected by a dependence of total accumulation only on the particle concentration gradient between blood and tumor, and therefore on blood half-life over time.[29] However, we found this to be significant by regression analysis only within the 40−100 nm range ($p < 0.02$), suggesting that there may be particle size effects for small diameters (20 nm in this case). To reconcile this, regression analysis was performed including size (nm^3) in addition to half-life as parameters, revealing a significant relationship for the 20 to 100 nm range ($p < 0.015$).

$$y = 794.907 + 0.768a - (7.053 \times 10^6)/(b^3)$$

where a is the half-life in minutes and b is the hydrodynamic diameter in nanometers. This suggests that accumulation of 40−100 nm particles is exclusively dependent on blood half-life, whereas the accumulation of particles in the 20 nm range depends on size and half-life (see Figure 2D). Further experimentation is required to determine the nature of this size-dependent effect. Nonetheless, this finding has a clear implication for particle design, namely that tumor accumulation of particles in the range of 40−100 nm is highly dependent on blood half-life and may allow accumulation to be optimized through parameters that determine blood PK.

The distribution of a therapeutic through a tumor mass will likely have a large impact on its effectiveness.[30] Hydrostatic pressure in a tumor mass typically decreases from the center to the periphery, the region where porous neovasculature is most dense.[29] Because of this, particles that enter the tumor through leaky vasculature may be carried by convection past the tumor periphery and into the sur-

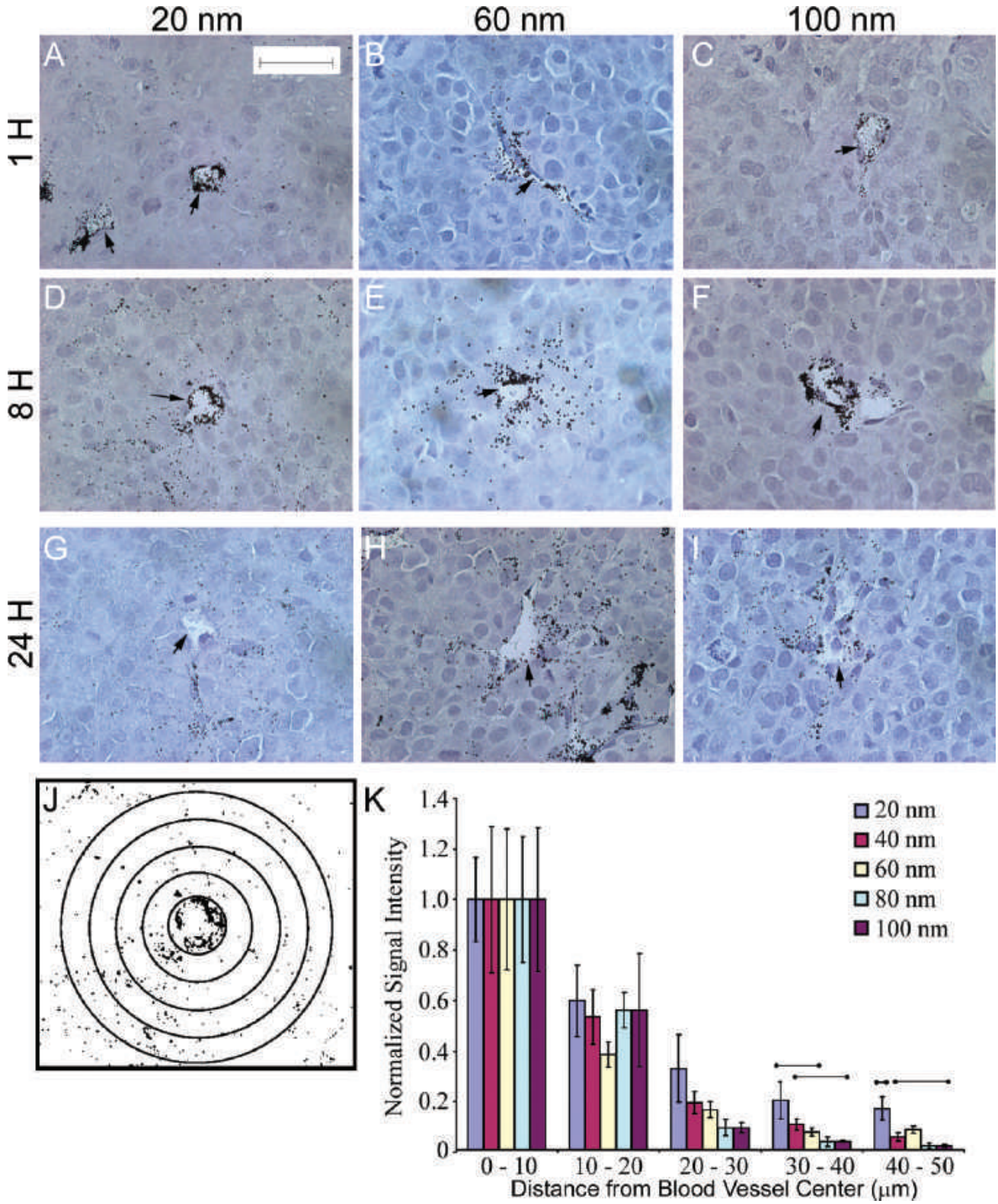

Figure 3. Particle size-dependent permeation of the tumor interstitial space. (A−I) Histological samples were obtained for 20, 60, and 100 nm particle sizes at 1, 8, and 24 h postinjection (HPI). Silver enhancement causes growth of the GNP, allowing their distribution relative to blood vessels (marked by arrows) to be visualized under bright-field microscopy (scale bar in A corresponds to 40 μm in all images). (A−C) 1 HPI, all particle sizes are localized in the perivascular space. (D−F) 8 HPI, a size-dependent trend emerges with 20 nm particles migrating far into the interstitial space, 60 nm particles showing limited migration, and 100 nm particles localized perivascularly. (G−I) 24 HPI, few 20 nm particles remain in the region surrounding the blood vessel, the 60 nm particles are seen migrating moderately far away from the blood vessel, and 100 nm particles have very limited migration. (J) ImageJ software was used to generate contrast-enhanced images for densitometry analysis. (K) Densitometry signal was quantified at 10 μm distances away from blood vessel centers 8 HPI and was normalized to the signal at 0−10 μm. Twenty nanometer particles had a significantly higher signal at distances further away from the vessel center, demonstrating a higher migration rate through the interstitial space ($n = 10$, $p < 0.05$).

rounding tissue, where they are likely to be cleared. This washout will be slowed by a restricted movement of particles through the tumor extra-cellular matrix (ECM) in a size-dependent manner.[29,31] Using a novel approach to visualize and quantify particle localization within a histology sample, we measured the size-dependent permeation of the interstitial space. Silver enhancement of tumor histological preparations causes particle growth by deposition of reactive silver. They can then be visualized under microscopic magnification, and quantified by contrast-enhanced densitometry analysis (see Figure 3). One hour postinjection, all particle sizes were similarly localized in the perivascular space with little penetration into the tumor mass (see Figure 3A−C and Figure S6 in Supporting Information). In contrast, 8 h postinjection we observed distinct trends in tumor permeation over the entire size range (see Figure 3D−F). The 20 nm particles (see Figure 3D) had permeated far from vessel centers, the 60 nm particles less so, and the 100 nm particles (see Figure 3F) were still localized in the perivascular region. This trend was further exaggerated at 24 h postinjection (see Figure 3G−I). Quantitative analysis of all five particle sizes at 8 h revealed a significant difference ($n = 10$, $p < 0.05$) in the migration of 20 nm particles versus all larger diameters (see Figure 3J−K). There was a general trend of decreased permeation as particle size increased. However, the difference between the four largest particle sizes was not statistically significant at any distance away from the blood vessel center. The relatively high permeation rate of 20 nm particles may have caused their clearance into surrounding tissues, which could account for their lower degree of accumulation. In contrast, the larger particle diameters may have benefited from a slower migration rate through the interstitial space, allowing greater accumulation.

To our knowledge, no study has yet examined the size-dependent permeation of nanoparticles through a tumor interstitial space. Dreher et al. made use of fluorescently labeled dextrans to demonstrate that vascular permeability and tumor permeation decrease as macromoleculer weight increases (3.3 kDa to 2 mDa).[32] Although the size and behavior of colloidal metal particles may be quite different from that of macromolecules, there are some interesting parallels with our results. They found that tumor accumulation increased with larger molecular weight (40−70 kDa or 11.2−14.6 nm) and attributed the poor accumulation of low molecular weight dextran (3.3−10 kDa) to a rapid rate of interstitial space permeation and clearance. It is difficult to draw conclusions across these studies, owing to the differences in macromolecule versus nanoparticle, and variability between tumor models. However, both studies have provided strong evidence that small particles and macromolecules are unsuitable for passive accumulation in the tumor compartment because of a high rate of interstitial space permeation.

We have systematically tested and described the in vivo behavior and tumor targeting capacity of sub-100 nm particles. This size range appears to be ideally suited to the design of tumor targeting vehicles as it allows for a broad range of blood PK, and tumor accumulation and permeation.

Specific tumor targeting behaviors for different applications can be achieved through particle design. For instance, we saw a striking size-dependent difference in tumor permeation that could be very useful toward different outcomes. If, for instance, the goal is to improve diagnostic sensitivity by maximizing the amount of a contrast agent delivered into the tumor compartment but localization within the tumor mass is unimportant, moderate particle cores protected with a large mPEG (5 or 10 kDa) brush layer having a final hydrodynamic diameter of 60−100 nm would provide excellent blood PK and tumor accumulation and could be used to localize leaky vasculature.

The design of vehicles for delivery of therapeutics is more complex. Large vehicles may behave similarly to our 100 nm particles with accumulation restricted to the perivascular space and little permeation into the tumor. This could be very useful for antiangiogenic therapy, but therapeutics aimed at the malignant cell bulk would be less effective. As a consequence, the greater volume provided by larger vehicles will be increasingly restricted from impacting cells far from leaky vasculature. This compromise makes a rational design of particle vehicles more complicated, especially in light of the variable nature of tumor growth. Nevertheless, we have observed a broad range of possible behaviors, from extremely restricted permeation (100 nm) to rapid permeation leading to poor accumulation (20 nm); 20−100 nm particles therefore offer a broadly tunable range for controlling vehicle behavior.

The trends described here will need to be tested in a wide range of tumor models and states of tumor growth before they can be applied universally. We did not observe a size-dependent restriction on sub-100 nm particle extravasation from the blood to the tumor. Sub-100 nm particles may be able to completely avoid such a restriction in tumors with highly permeable vasculature. Instead, the ability of a vehicle to either permeate the tumor interstitial space or remain at the perivascular space may be the most important factor that can be optimized through design. Future studies could aim to describe the variability in tumor extracellular matrix, its impact on particle permeation, and ultimately on effectiveness of a therapeutic or diagnostic agent. The fundamental knowledge provided here should provide a basis for such studies and for the rationale design of tumor targeting nanoparticles.

Acknowledgment. We thank Frank Giuliano and the technicians at the Division of Comparative Medicine, University of Toronto, for their support with this project. We also thank Kelvin So for his technical expertise, Barbara Alexander for her administrative support, and Dr. Young-In Kim at the University of Toronto for providing the MDA-MB-435 cell line. This study was funded by the Canadian Institute of Health Research, Canadian Foundation for Innovation, and Ontario Innovation Trust. S.D.P., H.C.F, and C.W. would like to acknowledge the National Sciences and Engineering Research Council of Canada for support through graduate student scholarships.

Supporting Information Available: Supporting Information is provided to describe detailed materials and methods.

We describe the cell and mouse lines used, particle synthesis and characterization, testing of particle stability, an ELISA detection format for quantification of pegylated particles in tissue samples, xenograft model and in vivo experimental setup, histology and silver enhancement technique for distribution of particles in tumor tissue, and statistics used. This material is available free of charge via the Internet at http://pubs.acs.org.

References

(1) Gao, X. H.; Yang, L. L.; Petros, J. A.; Marshal, F. F.; Simons, J. W.; Nie, S. M. *Curr. Opin. Biotechnol.* **2005**, *1*, 63–72.

(2) Akerman, M. E.; Chan, W. C. W.; Laakkonen, P.; Bhatia, S. N.; Ruoslahti, E. *Proc. Natl. Acad. Sci. U.S.A.* **2002**, *99* (20), 12617–12621.

(3) Babincova, M.; Sourivong, P.; Leszczynska, D.; Babinec, P. *Laser Phys. Lett.* **2004**, *9*, 476–478.

(4) Qian, X. M.; Peng, X. H.; Ansari, D. O.; Yin-Goen, Q.; Chen, G. Z.; Shin, D. M.; Yang, L.; Young, A. N.; Wang, M. D.; Nie, S. M. *Nat. Biotechnol.* **2008**, *1*, 83–90.

(5) Paciotti, G. F.; Myer, L.; Weinreich, D.; Goia, D.; Pavel, N.; McLaughlin, R. E.; Tamarkin, L. *Drug Delivery* **2004**, *3*, 169–183.

(6) Matsumura, Y.; Maeda, H. *Cancer Res.* **1986**, *12*, 6387–6392.

(7) Greish, K. *J. Drug Targeting* **2007**, *7*−*8*, 457–464.

(8) Maeda, H.; Fang, J.; Inutsuka, T.; Kitamoto, Y. *Int. Immunopharmacol.* **2003**, *3*, 319–328.

(9) Peer, D.; Karp, J. M.; Hong, S.; Farokhzad, O. C.; Margalit, R.; Langer, R. *Nat. Nanotechnol.* **2007**, *12*, 751–760.

(10) Davis, M. E.; Chen, Z.; Shin, D. M. *Nat. Rev. Drug Discovery* **2008**, *9*, 771–782.

(11) Lundqvist, M.; Stigler, J.; Elia, G.; Lynch, I.; Cedervall, T.; Dawson, K. A. *Proc. Natl. Acad. Sci. U.S.A.* **2008**, *38*, 14265–14270.

(12) Chithrani, B. D.; Ghazani, A. A.; Chan, W. C. W. *Nano Lett.* **2006**, *4*, 662–668.

(13) Liu, Y. L.; Shipton, M. K.; Ryan, J.; Kaufman, E. D.; Franzen, S.; Feldheim, D. L. *Anal. Chem.* **2007**, *6*, 2221–2229.

(14) Chung, T. H.; Wu, S. H.; Yao, M.; Lu, C. W.; Lin, Y. S.; Hung, Y.; Mou, C. Y.; Chen, Y. C.; Huang, D. M. *Biomaterials* **2007**, *19*, 2959–2966.

(15) Ding, L. H.; Stilwell, J.; Zhang, T. T.; Elboudwarej, O.; Jiang, H. J.; Selegue, J. P.; Cooke, P. A.; Gray, J. W.; Chen, F. Q. F. *Nano Lett.* **2005**, *12*, 2448–2464.

(16) Fujiwara, K.; Suematsu, H.; Kiyomiya, E.; Aoki, M.; Sato, M.; Moritoki, N. *J. Environ. Sci. Health, Part A: Toxic/Hazardous Substances & Environmental Engineering* **2008**, *10*, 1167–1173.

(17) Jiang, W.; Kim, B. Y. S.; Rutka, J. T.; Chan, W. C. W. *Nat. Nanotechnol.* **2008**, *3*, 145–150.

(18) Geng, Y.; Dalhaimer, P.; Cai, S.; Tsai, R.; Tewari, M.; Minko, T.; Discher, D. E. *Nat. Nanotechnol* **2007**, *4*, 249–255.

(19) Shukla, R.; Bansal, V.; Chaudhary, M.; Basu, A.; Bhonde, R. R.; Sastry, M. *Langmuir* **2005**, *23*, 10644–10654.

(20) Dunn, S. E.; Brindley, A.; Davis, S. S.; Davies, M. C.; Illum, L. *Pharm. Res.* **1994**, *7*, 1016–1022.

(21) Jackson, H.; Muhammad, O.; Daneshvar, H.; Nelms, J.; Popescu, A.; Vogelbaum, M. A.; Bruchez, M.; Toms, S. A. *J. Neurooncol.* **2008**, *2*, 243–243.

(22) Mosqueira, V. C.; Legrand, P.; Morgat, J. L.; Vert, M.; Mysiakine, E.; Gref, R.; Devissaguet, J. P.; Barratt, G. *Pharm. Res.* **2001**, *10*, 1411–1419.

(23) Fang, C.; Shi, B.; Pei, Y. Y.; Hong, M. H.; Wu, J.; Chen, H. Z. *Eur. J. Pharm. Sci.* **2006**, *1*, 27–36.

(24) Hobbs, S. K.; Monsky, W. L.; Yuan, F.; Roberts, W. G.; Griffith, L.; Torchilin, V. P.; Jain, R. K. *Proc. Natl. Acad. Sci. U.S.A.* **1998**, *8*, 4607–4612.

(25) Yuan, F.; Dellian, M.; Fukumura, D.; Leunig, M.; Berk, D. A.; Torchilin, V. P.; Jain, R. K. *Cancer Res.* **1995**, *17*, 3752–3756.

(26) Soo Choi, H.; Liu, W.; Misra, P.; Tanaka, E.; Zimmer, J. P.; Itty Ipe, B.; Bawendi, M. G.; Frangioni, J. V. *Nat. Biotechnol.* **2007**, *10*, 1165–1170.

(27) Fischer, H. C.; Chan, W. C. *Curr. Opin. Biotechnol.* **2007**, *18* (6), 565–571.

(28) Bhujwalla, Z. M.; Artemov, D.; Natarajan, K.; Ackerstaff, E.; Solaiyappan, M. *Neoplasia* **2001**, *2*, 143–153.

(29) Jain, R. K. *Annu. Rev. Biomed. Eng.* **1999**, 241–263.

(30) Steyger, P. S.; Baban, D. F.; Brereton, M.; Ulbrich, K.; Seymour, L. W. *J. Controlled Release* **1996**, *1*, 35–46.

(31) Pluen, A.; Netti, P. A.; Jain, R. K.; Berk, D. A. *Biophys. J.* **1999**, *1*, 542–552.

(32) Dreher, M. R.; Liu, W. G.; Michelich, C. R.; Dewhirst, M. W.; Yuan, F.; Chilkoti, A. *J. Natl. Cancer Inst.* **2006**, *5*, 335–344.

NL900031Y